Effective Diffusivities of Gases in a Reconstructed Porous Body
Proceedings of European Congress of Chemical Engineering (ECCE-6)
Copenhagen, 16–20 September 2007

Effective Diffusivities of Gases in a Reconstructed Porous Body

Pavel Čapek[a1], Vladimír Hejtmánek[b], Libor Brabec[c], Arlette Zikánová[c], Milan Kočiřík[c]

[a] *Institute of Chemical Technology, Prague, Technická 5, 16628 Prague, CZ*
[b] *Institute of Chemical Process Fundamentals ASCR, v.v.i, Rozvojová 135, 16502 Prague, CZ*
[c] *J. Heyrovský Institute of Physical Chemistry ASCR, v.v.i., Dolejškova 3, 18223 Prague, CZ*

Abstract

Two models of a porous body, a 3D replica obtained by stochastic reconstruction and a random pore network, were evaluated with reference to the effective diffusivity of gases. The stochastic reconstruction technique employs the limited morphological information that was extracted from images of 2D cuts through the porous medium. The pore network was derived in such a way that the total porosity, pore-size function, mean coordination number, and mercury intrusion curve agreed well with experiment. A simulator of steady diffusion flow in the pore network slightly overestimated the effective diffusivity while the direct calculation of the effective diffusivity by exploiting random-walk simulation in the 3D replica delivered a value that was lower than its experimental counterpart. However, both deviations were acceptable.

Key words: stochastic reconstruction, pore network, random walk, diffusivity

1 Introduction

Disorder media, particularly porous solids, are often used in many fields of science and technology. Understanding the relationships between their microstructure and mass transport is therefore of great theoretical and practical interest. As a result, numerous works including new theoretical concepts, novel experimental techniques and reliable experimental data have appeared in the literature. Abstract schemes (e.g. dusty-gas model (Mason

[1]Corresponding author. e-mail: pavel.capek@vscht.cz

et al., 1967)) or geometry-based models (capillary models, e.g. (Johnson and Stewart, 1965)) can be found among early approaches to the microstructure representation. These models, sometimes classified (Sahimi et al., 1990) as *continuum*, always contain a few adjustable parameters (e.g. tortuosity and the mean pore radius) that reflect transport properties of a porous body. In spite of much progress has been made using them, there is a strong need for a more detailed microstructure description that would be free of adjustable parameters and suitable for the prediction of macroscopic properties, such as effective diffusivity, permeability and capillary pressure curves, from the first principles. Furthermore, newer investigations (e.g. Sahimi et al., 1990; Hollewand and Gladden, 1992; Keil, 1999) cast doubt on the application of the continuum models and on the concept of the adjustable parameters (tortuosity) under conditions that are different from those used in experiments designed for the parameter adjustment. In this context *discrete* models (Sahimi et al., 1990) of the disorder media offer a promising way to elucidate the aforementioned relationships.

The prediction of the macroscopic properties from the microscopic origin needs two main steps:

1. furnishing the discrete models with the requisite geometrical and topological information about the complex microstructure of the medium,

2. an exact or approximate solution of the mass, momentum and energy balances that govern the transport phenomenon under study.

The first step is nowadays feasible in many cases due to the development of efficient algorithms of image analysis, which are capable of processing data from various sources, such as light, electron, or scanning laser confocal (Fredrich et al., 1995) microscopy, magnetic resonance imaging (Baldwin et al., 1996), and X-ray computed tomography (Spanne et al., 1994). In the absence of the experimental 3D volume data, delivered, for instance, by X-ray computed tomography, stochastic reconstruction has been found (Yeong and Torquato, 1998a,b; Manwart and Hilfer, 1999) to be useful for mapping a real sample onto a 3D regular array of voxels (a phase function) with adequate resolution. Regardless of the pore structure reconstruction technique chosen, a unit cell of the reconstructed porous body (a 3D replica) can serve as the computational domain for the direct calculation of the macroscopic properties, i.e. for the realization of the second step. Alternatively, reconstructed pore space can be transformed onto an equivalent random pore network. A network approach to an estimation of effective diffusivity or permeability involves the substantial simplification of pore geometry. Then, expressions for the flow rates in individual pores are derived and microscopic concentration

profiles are determined by applying the law of conservation of mass in all network nodes. Both approaches have advantages and shortcomings. The direct calculation takes advantage of detailed information on pore space topology and morphology. Due to limitations of computer resources, a 3D replica may not be large enough; consequently, macroscopic properties may reveal the undesirable dependence on its size. Pore network models simplify pore geometry (and pore space topology) and, thus, can simulate larger unit cells, demanding less computer resources. Relatively few papers (e.g. Liang et al., 2000b; Bekri et al., 2000; Talukdar et al., 2002) comparing both approaches have only appeared so far. Therefore, it would be worth investigating it further.

The first objective of this paper is to reconstruct stochastically a porous body and to derive an equivalent random pore network. The second objective is to compute effective diffusivities of gases in these models of the porous body and to compare them with the experimental effective diffusivity. The effective diffusivity in the reconstructed porous body will be computed directly by random-walk simulation. The same quantity in the pore network will be determined by the simultaneous solution of a large set of non-linear equations that result from the application of the law of conservation of mass to each network node. This work is an extension of our previous work (Čapek et al., in press), in which effective permeability and diffusivity have been modelled using a pore network of different geometry and topology.

2 Models of a Porous Body

Two models of an α-alumina sample with the total porosity $\phi = 0.404$ are presented in this work. A method of the 3D stochastic reconstruction based on the limited statistical information extracted from images of 2D, randomly-oriented cuts through the porous body was applied to reproduce the microstructure of the sample. A 3D replica (the first model) served as the main source of data for the construction of the second model based on a random pore network in which chambers (cavities) were connected through convergent-divergent throats (necks).

2.1 Microstructural Descriptors

The structure of a two-phase porous medium is completely defined (Torquato, 2002) in terms of the indicator function, $\mathcal{I}(\vec{x})$, for the void phase

$$\mathcal{I}(\vec{x}) = \begin{cases} 1, & \text{if } \vec{x} \text{ belongs to the pore space} \\ 0, & \text{otherwise} \end{cases} \tag{1}$$

where $\vec{x}$ is the position vector. In the 2D digitized representation of a porous medium, the position vector $\vec{x}$ takes discrete values $\vec{x} = (\mathsf{i}a, \mathsf{j}a)$ determined by a square lattice with $\mathsf{i} = 0, \ldots, l_x - 1$ and $\mathsf{j} = 0, \ldots, l_y - 1$ and the size $l_x \times l_y$. Similarly, in the 3D digitized media the discrete values of the position vector $\vec{x} = (\mathsf{i}a, \mathsf{j}a, \mathsf{k}a)$ are defined by a simple cubic lattice and the size $l_x \times l_y \times l_z$. The lattice constant, a, corresponds to the pixel or voxel resolution.

For statistically homogeneous (invariant under translation of the spatial coordinates) and stationary media, the volume fraction of the void phase (total porosity) is defined as

$$\phi = \langle \mathcal{I}(\vec{x}) \rangle \tag{2}$$

where angular brackets denote an ensemble average. Equation (2) is also known as the definition of the one-point probability function for those media. The two-point probability function for the void phase is defined by

$$\mathcal{S}(\vec{x}_1, \vec{x}_2) = \langle \mathcal{I}(\vec{x}_1)\mathcal{I}(\vec{x}_2) \rangle \tag{3}$$

where $\vec{x}_1$ and $\vec{x}_2$ are two arbitrary points in the system. If a porous medium is also isotropic (invariant under rotation), the two-point probability function depends only on the distance $u = |\vec{x}_1 - \vec{x}_2|$ and, thus, $\mathcal{S}(\vec{x}_1, \vec{x}_2) = \mathcal{S}(u)$.

Another microstructural descriptor is the lineal-path function, $\mathcal{L}(\vec{x}_1, \vec{x}_2)$, for the void phase, which is defined (Torquato, 2002) as the probability of finding a line segment spanning from $\vec{x}_1$ to $\vec{x}_2$ that lies entirely in the void phase. In an isotropic medium, the lineal-path function depends only on u and can be expressed simply as $\mathcal{L}(u)$.

For the characterization of three-dimensional porous media, the pore-size probability density function, $\mathcal{P}(\delta)$, may be used. The function $\mathcal{P}(\delta)$ for the void phase of an isotropic medium is defined (Torquato, 2002) as the probability that a randomly chosen point in the void phase lies at the distance between δ and $\delta + \mathrm{d}\delta$ from the nearest pore-solid interface. The function $\mathcal{P}(\delta)$ is an intrinsically three-dimensional descriptor and, therefore, cannot be obtained from the images of two-dimensional cuts through the solid. The associated cumulative distribution function, $\mathcal{F}(\delta)$, is the fraction of the pore space that has a pore radius greater than δ

$$\mathcal{F}(\delta) = \int_{\delta}^{\infty} \mathcal{P}(u)\mathrm{d}u \tag{4}$$

The mean pore size, $\langle \delta \rangle$, can be defined in terms of $\mathcal{F}(\delta)$

$$\langle \delta \rangle = \int_{0}^{\infty} \mathcal{F}(\delta)\mathrm{d}\delta \tag{5}$$

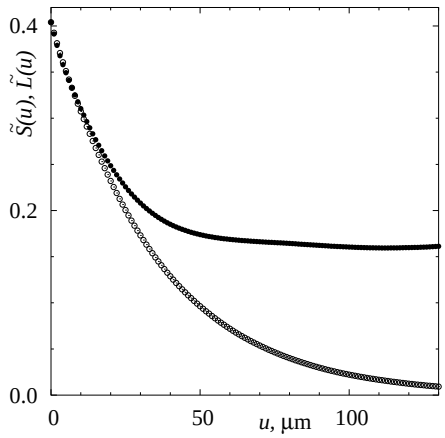

Figure 1: Reference microstructural descriptors: • – $\widetilde{\mathcal{S}}(u)$ and ⊙ – $\widetilde{\mathcal{L}}(u)$.

2.2 2D Image Processing

After drying, cylindrical pellets (5 mm height × 5 mm diameter, made of alumina grains with the mean particle size of 29.2 μm) were impregnated under vacuum with epoxy resin Araldite. The hardened epoxy resin blocks were cut, ground and polished to achieve the smooth surface. Series of back-scatter scanning electron images of cross-sections through the medium were recorded in an appropriate size and resolution. Twenty images of the unique size of 1280 × 960 pixels at the pixel resolution $a = 1\,\mu$m were selected for analysis. The discrete level of grey intensity always spanned the interval of $[0, 255]$ in all images. Each raw image was subjected to a sequence of operations that involved median filtering and image segmentation, i.e. the determination of the grey-level threshold.

The segmented images were sampled in the two principal directions. The functions $\mathcal{S}(u)$ and $\mathcal{L}(u)$ were found to be nearly independent of the direction chosen. The reference functions $\widetilde{\mathcal{S}}(u)$ and $\widetilde{\mathcal{L}}(u)$ for the purpose of 3D stochastic reconstruction (Fig. 1) were determined by averaging the functions obtained from the individual images.

2.3 3D Stochastic Reconstruction

A 3D replica of the porous body, conforming to the reference and simulated microstructural descriptors, was generated by the simulated annealing technique (Aarts and Korst, 1989; Press et al., 1992). This technique of combinatorial minimization gradually transforms a high-energy configuration of void and solid voxels into a minimum-energy configuration. The objective func-

tion ("energy" of the digitized system) E was given by the sum of squared deviations between the reference and simulated functions:

$$E = \sum_{i=1}^{3} \sum_{u=0}^{130} \left[\left(\widetilde{\mathcal{S}}(u) - \mathcal{S}_i(u) \right)^2 + \left(\widetilde{\mathcal{L}}(u) - \mathcal{L}_i(u) \right)^2 \right] \tag{6}$$

The simulated functions were calculated in the three principal directions ($i = 1, 2, 3$), applying periodic boundary conditions. In (6) we assumed that the deviations between the reference and calculated functions were negligible beyond the distance of $130\,\mu$m. It was justified: $\widetilde{\mathcal{S}}(u)$ first declined below its log-range value of ϕ^2 at $u = 86\,\mu$m and $\widetilde{\mathcal{L}}(u)$ approached zero when $u > 130\,\mu$m (Fig. 1).

At the beginning of 3D reconstruction, a random configuration of pore and solid voxels is formed with the total porosity, ϕ, on the simple cubic lattice of size $l_x \times l_y \times l_z = 256 \times 256 \times 256$. At each iteration step k, a new configuration is generated by selecting two voxels of the different phase at random and exchanging their phase function values. This exchange slightly alters $\mathcal{S}_i(u)$ and $\mathcal{L}_i(u)$ and, thus, results in the energy difference $\Delta E^{(k)} = E^{(k)} - E^{(k-1)}$. A voxel exchange is accepted with a probability p_k given by the Metropolis rule (Aarts and Korst, 1989)

$$p_k\left(\Delta E^{(k)}\right) = \begin{cases} 1\,, & \text{if } \Delta E^{(k)} \leq 0 \\ \exp\left(-\Delta E^{(k)}/\vartheta\right)\,, & \text{if } \Delta E^{(k)} > 0 \end{cases} \tag{7}$$

where ϑ is a control parameter representing the system "temperature". If the voxel exchange is rejected, the phase function values are restored and the previous configuration is left unchanged. The temperature is lowered after a certain number of iteration steps, referred to as a Markov chain (Aarts and Korst, 1989). 92×10^4 iteration steps were found to be sufficient for equilibrating the system at each fixed temperature. The initial temperature and the rate of temperature reduction are described by an annealing schedule. Modern implementations of simulated annealing prefer adaptive schedules that can cool at optimum speed. For instance, the "heat capacity" method, applied here, cools in constant energy slices (Frost and Heineman, 1997). The algorithm by Aarts and Korst (1989) was employed for estimation of the initial temperature so that the acceptance probability for the first Markov chain would be 0.95. The algorithm was terminated when $E < 10^{-7}$.

An approximation to $\mathcal{P}(\delta)$ was computed by placing a random point in the reconstructed pore space and measuring its distance δ to the nearest point on the phase interface, which was modelled by faces of cubic voxels. This procedure was repeated for a large number of random points in the pore space. The function $\mathcal{P}(\delta)$ was then obtained by discretizing the distances δ

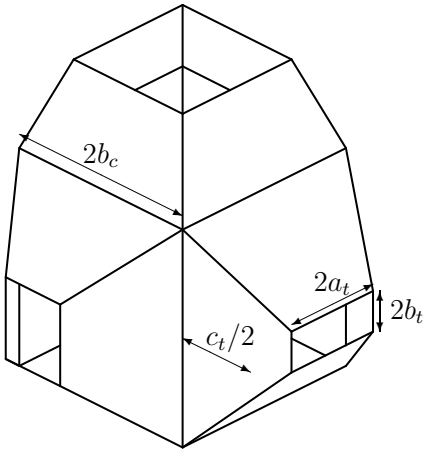

Figure 2: Schematic representation of a cubic chamber and halves of three adjacent throats. The chamber volume, V_c, is determined by the chamber edge size: $V_c = 8b_c^3$. For the throat sizes, a_t and b_t, the following inequalities hold: $a_t \leq b_c$ and $b_t < b_c$ (a self-consistency limitation). The throat aspect ratio, $\lambda = a_t/b_t$, satisfies the inequality: $\lambda \geq 1$

and dividing by the total number of random points placed into the pore space. Integration of the resulting function according to (4) gave an approximation to $\mathcal{F}(\delta)$.

2.4 Random Pore Network

The reconstructed pore space was analysed and transformed onto a 3D pore network of irregular topology. Since visual inspection of the 3D replicas revealed that the pore space was well represented by pores of convergent-divergent shapes, a chamber-and-throat network was chosen for the transformation. Each network throat was formed by two obelisks, mutually connected. Their larger, square bases took the sizes of adjacent cubic chambers; the smaller, rectangular bases of the same size represented the narrowest throat cross-section area (Fig. 2).

The preliminary construction of the pore network showed that the chamber size distribution (CSD) and throat size distribution (TSD) had to overlap strongly; therefore, the common procedure of the network construction (Constantinides and Payatakes, 1989; Tsakiroglou and Payatakes, 1990) could not be employed. Furthermore, the combination of the relatively high total porosity (0.404) and the wide CSD, related to $\mathcal{F}(\delta)$, made the transformation of highly irregular pore space into cubic chambers arranged in nodes of a cu-

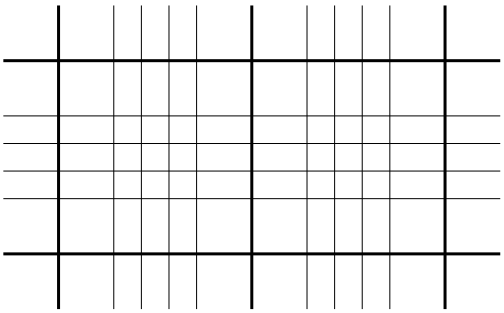

Figure 3: Two-dimensional cut through a three-dimensional network, chambers of which are arranged in nodes (i.e. in intersections of lines) of two cubic arrays.

bic array difficult. A few network realizations confirmed that chamber sizes (volumes) could not be assigned to the network nodes completely at random, because no two adjacent chambers were allowed to intersect. The introduction of the negative chamber-to-chamber correlation (i.e. large chambers were surrounded by small chambers (Tsakiroglou and Payatakes, 1993)) did not result in any consistent network. Instead of it, chambers were hierarchically arranged in nodes of two cubic arrays. "Fine" cubic arrays sharing a common distance between two arbitrary nodes were embedded in unit cells of the "coarse" cubic array (thin and thick lines in Fig. 3 respectively). Each fine array was attached to the coarse array via bonds (throats) connecting auxiliary nodes (chambers) placed in six faces of the unit cell and external nodes of the fine array. The fine array size (number of the fine array nodes in the unit cell of the coarse array, $4 \times 4 \times 4$ in Fig. 3) was an important parameter of the network. Chamber volumes were assigned to the network nodes as follows. The domain of the chamber volume distribution (CVD) was divided into three parts. Chamber volumes selected at random from the upper part of the domain were assigned to the nodes located in the intersections of thick lines (Fig. 3). Then chamber volumes corresponding to the middle part of the CVD domain were assigned to the nodes represented by the intersections of thick and thin lines. Finally, chamber volumes from the lower part of the CVD domain were assigned to the remaining nodes. The feasibility of such a network construction depends on the total porosity, CVD and fine array size. It should be emphasized that the fine array size need not be necessarily $4 \times 4 \times 4$ as it is depicted in Fig. 3. The node distances of the fine and coarse arrays constrained sizes and shapes of the chambers located in the intersections of the thick and thin lines. These chambers were allowed to have the rectangular parallelepiped shape for the network

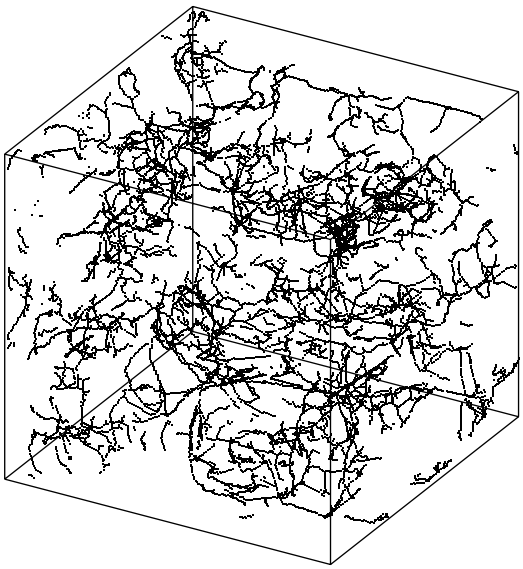

Figure 4: Skeleton of the reconstructed pore space. The full size ($256 \times 256 \times 256$ voxels) of the sample is shown.

construction to be feasible. It also explains why the CVD was preferred to the CSD. This procedure introduced the positive chamber-to-chamber correlation (Tsakiroglou and Payatakes, 1991) in the pore network, i.e. large chambers were preferentially surrounded by chambers of similar sizes.

A cubic network has regular topology with the coordination number (i.e. number of bonds per node) of 6. However when a cubic network is to be of irregular topology, its mean coordination number, $\bar{\omega}$, has to be reduced by removing bonds selected at random. Then the coordination numbers, ω, of individual chambers are equal to random integers between 1 and 6. In this work $\bar{\omega}$ was estimated from a skeleton of the reconstructed pore space. The pore space skeleton (Fig. 4) was determined using a fully parallel 3D thinning algorithm (Min Ma and Sonka, 1996), and was used as a graph, edges and vertices of which were composed of voxels with two 26-adjacent neighbours and three or more 26-adjacent neighbours respectively. This simple definition of edges and vertices, also used by Thovert et al. (1993), resulted in $\bar{\omega} = 3.9$. An advanced algorithm of pore space partitioning based on morphological skeletonization (Liang et al., 2000a) will be considered in our future work.

Since the chamber and throat size distributions overlapped, a certain level of the positive chamber-to-throat (c–t) correlation had to be assumed. An algorithm for the efficient assignment of throat sizes b_t to network bonds was

implemented by the following way. A number ("vote") Υ_{ij} evaluated on the basis of adjacent chamber sizes, b_{ci} and b_{cj},

$$\Upsilon_{ij} = \min\left(b_{ci}, b_{cj}\right) \tag{8}$$

was assigned to each bond in the network. Then the bonds were ranked in descending order according to their votes Υ_{ij}. A number of the throat sizes equal to the total number of network bonds was generated according to the TSD given and was sorted in descending order. This set of the throat sizes was partitioned in a number of classes (say, 8192), each containing the throat sizes within a narrow interval. The widest throats belonging to the first class were scattered at random among the network bonds in such a way that no throat size was greater than the corresponding vote Υ_{ij}, i.e. the self-consistency limitation was fulfilled. This step was iterated for next classes until a number of the remaining throat sizes was zero. The process of the throat scattering depended on a free positive parameter ζ that could be varied within $(0, 1]$ to yield the desirable level of correlation. he smaller the value of ζ, the stronger the c–t correlation was. When the distributions overlapped, a certain level of the c–t correlation was unavoidable regardless of a value of ζ. Periodic boundary conditions for the throat sizes were applied in three principal directions of the network.

For the strongly overlapping CSD and TSD, this implementation of the throat size assignment algorithm was found to deliver no mistakes in comparison with the procedures suggested by Tsakiroglou and Payatakes (1991), and later by Burganos and Payatakes (1992).

In order to raise randomness in pore morphology we drew random values of λ (Fig. 2) from the uniform distribution in the interval $[1, 1.2]$. This relatively narrow interval enabled the values of λ to be independent of values of b_t.

After assigning chamber volumes to network nodes and throat sizes to network bonds and making specification of connectivity, the distance between the centres of gravity of two adjacent chambers was adjusted so that the total porosity of the network could agree with that of the prototype. Note that both chambers and throats contributed to the total pore volume.

2.4.1 Estimation of pore network parameters

The function $\mathcal{F}(\delta)$ of the 3D replica provided decisive information for the adjustment of the network parameters, particularly the CVD and TSD. This adjustment was carried out iteratively by matching $\mathcal{F}(\delta)$ of the 3D replica and the pore network generated in each iteration. Since numerical experiments indicated that $\mathcal{F}(\delta)$ for the network void phase was more sensitive

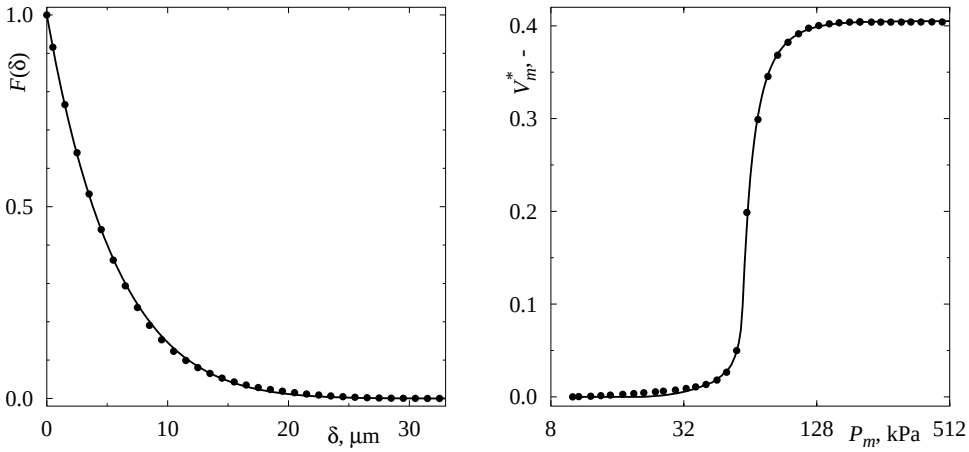

Figure 5: The best approximations (—) of $\mathcal{F}(\delta)$ and capillary pressure curve obtained in the iterative network construction are compared with experimental dependences (•). The experimental function $\mathcal{F}(\delta)$ corresponds to the 3D replica.

to perturbations of the CVD than to perturbations of the TSD, a modified procedure was employed to estimate the TSD more precisely. In this procedure systematic modifications of the TSD were performed in such a way that the calculated mercury intrusion curve well fitted the experimental one. Tsakiroglou and Payatakes (2000) suggested a similar algorithm for the refinement of the TSD obtained by means of the serial sectioning analysis of double pore casts.

The common model of the mercury porosimetry assumes that mercury intrusion is solely controlled by constriction sizes (Sahimi, 1995). We accepted a more sophisticated model of the critical capillary pressure (Tsakiroglou and Payatakes, 1990), which also takes into account equilibrium at entrances to chambers. In the case of our particular pore geometry and the intrusion contact angle of $2\pi/9$ it meant that the critical capillary pressure in a throat was dependent on a_t, b_t and c_t, and the sizes of adjacent chambers (b_{ci} and b_{cj}). The mercury intrusion algorithm implemented in our simulator is usually called invasion percolation (Sahimi, 1995). In all mercury porosimetry runs the simulated cubic particle was immersed in mercury so that mercury could invade the pore space through its six faces. The pore volume, V_m, invaded by mercury was related to the particle volume V_p: $V_m^\star = V_m/V_p$, i.e. $\lim_{P_m\to\infty} V_m^\star = \phi$ where P_m is the external pressure of mercury.

The iterative construction of the chamber-and-throat network can be summarized as follows:

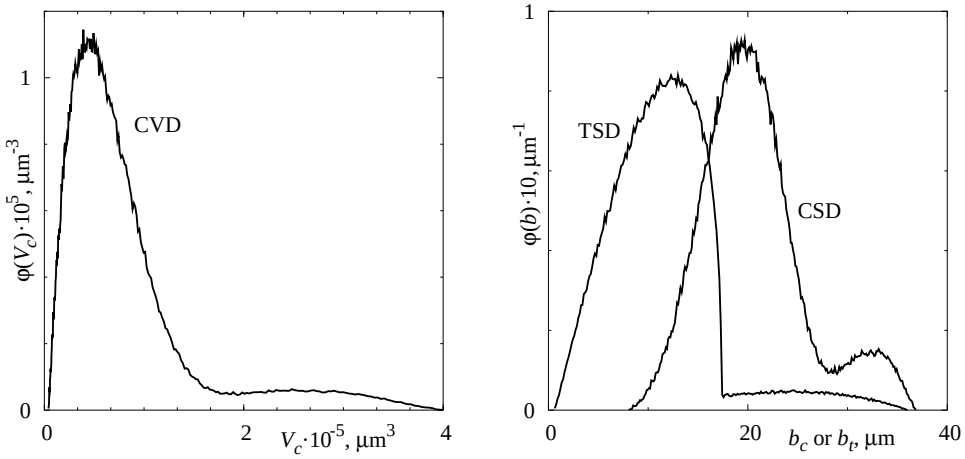

Figure 6: Number density functions of CVD, $\varphi(V_c)$, the corresponding CSD, $\varphi(b_c)$, and TSD, $\varphi(b_t)$.

1. The CVD domain was derived from the domain of $\mathcal{F}(\delta)$ (Fig. 5). The network connectivity was defined by setting $\bar{\omega} = 3.9$.

2. Initial approximations of the CVD and TSD, based on the previous experience (Čapek et al., in press; Čapek and Hejtmánek, 2004), were accepted.

3. The pore space of the network model was sampled to get an approximation of $\mathcal{F}(\delta)$. This approximation was compared with the reference function characterizing the reconstructed pore space (Fig. 5).

4. Mercury intrusion was simulated and the resulting capillary capillary pressure curve, $V_m^\star = f(P_m)$, was compared with the experimental (reference) one (Fig. 5).

5. If either the calculated $\mathcal{F}(\delta)$ or the simulated capillary pressure curve did not match the reference one, the CVD and TSD were altered and a new realization of the pore network was generated.

6. The steps (3–5) were repeated until the calculated functions did fit well the reference ones.

The preliminary construction (step 2 in the above list) revealed that the CVD had to be skewed strongly, with a long tail extending out towards more positive V_c. The asymmetric CVD (Fig. 6) was modelled by combination of two beta probability distributions. The shape and domain span of the

CVD made the fine array size of $3 \times 3 \times 3$ essential. The CVD domain was divided into the three sub-domains by two internal points of $133810\,\mu\mathrm{m}^3$ and $321065\,\mu\mathrm{m}^3$, respectively. This implied that a number of the chamber volumes related to the first peak of the number density function $\varphi(V_c)$ was scattered over the fine array nodes. Chamber volumes from the middle CVD sub-domain were randomly assigned to the nodes located in the intersections of the thin and thick lines (Fig. 3), chamber volumes from the upper CVD sub-domain to the coarse array nodes. A similar combination of two beta probability distributions was found to be useful for modelling the TSD, which had the positive skewness as well (Fig. 6). The asymmetric TSD was necessary for the calculated mercury intrusion curve to fit well the experimental curve in its low-pressure part ($P_m < 48\,\mathrm{kPa}$). The parameter ζ controlling the level of the positive c–t correlation was always equal to one, i.e. the observed c–t correlation stemmed only from the presence of the two overlapping distributions.

Since the mean pore size was large enough ($\langle\delta\rangle = 5.17\,\mu\mathrm{m}$), the pore network of $72 \times 72 \times 72$ nodes represented the cubic particle whose external size ($d_p = 5.08$ mm) was very close to the real particle diameter and height ($5\,\mathrm{mm} \times 5\,\mathrm{mm}$). That number of nodes also ensured the excellent statistical stability of simulated quantities, which was confirmed by a few network realizations.

3 Simulation of Effective Diffusivities

Effective diffusivities were simulated in the region of continuum, i.e. it was assumed that the number of collisions of the molecules among themselves is much higher than the number of collisions with pore walls (hence the Knudsen number tends to zero). For each model of the porous solid, a corresponding simulator was derived. A random-walk simulator that was based on calculation of the mean-squared displacement versus time was applied to estimate directly the effective diffusivity in the 3D replica. In the case of the network model mass and momentum balances for individual pores were solved firstly; secondly, resulting total diffusion flow was reduced to the effective diffusivity.

3.1 Effective Diffusivity in the Stochastic Replica

Methods of random-walk simulation (Sahimi and Stauffer, 1991; Ioannidis et al., 1997; Burganos, 1998; Kainourgiakis et al., 2005) use the well-known relationship between the mean squared displacement $\langle\xi^2\rangle$ of a walker, exe-

cuting a random walk in the medium, and time τ:

$$D_e^m = \lim_{\tau \to \infty} \frac{\langle \xi^2 \rangle}{6\tau} \tag{9}$$

where D_e^m is the effective diffusivity of the walker in the region of continuum.

A large number of random walkers were considered for calculation of the limit (9). Each random walk started by placing a random walker at the centre of a void-phase voxel, whose coordinates were selected at random. If such a voxel belonged to an isolated cavity, a new location was generated. Then, the walker was allowed to jump from its current location to the centre of one of its 26 nearest neighbouring voxels with an equal probability of 1/26. The walker's jump took an amount of time $\Delta\tau$, which was chosen to obey Einstein's relation $r^2 = 6D^m\Delta\tau$ where D^m is the bulk diffusivity of the walker and r is the Euclidean distance between two successive locations of the walker. Depending on the relative location of the neighbouring voxels, the Euclidean distance could take the values of a, $a\sqrt{2}$, or $a\sqrt{3}$. If the neighbouring voxel selected for the next location of the walker belonged to the solid matrix, the walker formally jumped to the void-solid interface and back to its previous location. Such a formal jump increased the total time by $\Delta\tau$ as well. Jumps through pore orifices were resolved by applying the periodic boundary conditions, i.e. the walker was allowed to move in one of the six cells surrounding the central cell. Since the medium was digitized and since the ratio of the effective to the bulk diffusivity was of interest, the dimensionless total time $\tau^\star = 6D^m\tau a^{-2}$ was introduced and Equation (9) was expressed in the form:

$$\frac{D_e^m}{D^m} = \lim_{\tau^\star \to \infty} \frac{\langle \xi^2 a^{-2} \rangle}{\tau^\star} \tag{10}$$

In this equation the mean squared displacement was measured in the integer coordinates of the phase function. Each time step added 1, 2, or 3 to the dimensionless total time, which had to be large enough to make sure that the walker felt the effect of the void-solid interface details. Specifically, the number of time steps proportional to the number of void voxels in the replica ($\approx 7\times10^6$) and 5000 random walkers provided a good estimate of the effective diffusivity.

3.2 Diffusion Flow in the Pore Network

The scheme of a representative single pore is shown in Fig. 7. The single pore consisted of three segments, a convergent-divergent throat and halves of both adjacent chambers. Steady diffusion flow rates in a single pore under

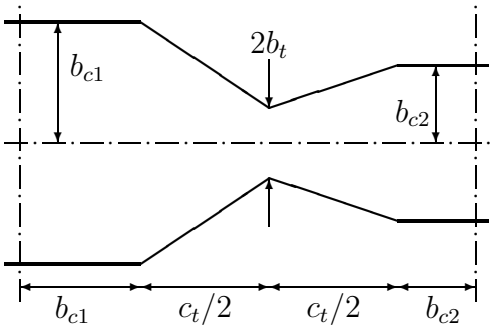

Figure 7: Geometry of a single pore consisting of a convergent–divergent throat and halves of both adjacent chambers

isothermal conditions were calculated on the basis of state variables located in chamber centres. If any of the adjacent chambers had the rectangular parallelepiped shape, its actual geometry was considered in expressions for the diffusion flow rates.

The transport of binary gaseous mixtures in a single capillary can be described by the Maxwell-Stefan constitutive equations (Bird et al., 1960). If a binary mixture consisting of gases A and B is considered and the ratio of diffusion fluxes obeys Graham's law (Mason and Evans III, 1969), a set of two constitutive equations can be replaced by a single constitutive equation. Note that the validity of Graham's law implies the uniformity of the total pressure in a porous medium as well as transport of inert gases. Taking into account this fact we expressed the diffusion molar flow rate, $\dot{n}_{12}$, of a gas A in a single pore as

$$\dot{n}_{12} = \left[\frac{1}{g_d D_{AB}} + \frac{\alpha}{g_d D_{AB}} \frac{y_1 + y_2}{2} \right]^{-1} \frac{P}{R_g T} (y_1 - y_2) \tag{11}$$

where y_1 and y_2 are the mole fractions of A in the chambers 1 and 2 respectively, P is the total pressure, R_g is the gas constant, T is the thermodynamic temperature, D_{AB} is the bulk binary diffusion coefficient of the pair A–B, and $\alpha = \sqrt{[M_A/M_B]} - 1$ is a modified ratio of molecular weights M_A and M_B. For the single-pore conductance, g_d, the following expression was derived

$$g_d = 4 \left[\frac{1}{b_{c1}} + \frac{c_t}{2b_{c1}\sqrt{(a_t b_t)}} + \frac{c_t}{2b_{c2}\sqrt{(a_t b_t)}} + \frac{1}{b_{c2}} \right]^{-1} \tag{12}$$

Bulk binary diffusion coefficients can be found for many gaseous mixtures in the review article by Mason and Marrero (1972).

In pore networks single pores are connected at network nodes. Steady molar flow rates that enter a node must be equal to the molar flow rates leaving the node, i.e. mass must be conserved. The unknown chamber (node) pressures were determined by simultaneous solution of $72 \times 72 \times 72 = 373248$ non-linear equations, which resulted from the application of the law of conservation of mass to each chamber, namely

$$\sum_i \dot{n}_{ij} = 0\,, \qquad j = 1, \ldots, 373248 \tag{13}$$

where $\dot{n}_{ij}$ are the molar flow rates between the jth chamber and the adjacent chambers denoted by appropriate subscripts i.

In the standard experimental setup a porous pellet is mounted in an impermeable (metallic) disc of a measuring cell. Both disc sides are exposed to fluid phases of different composition; consequently, dependences of steady diffusion fluxes on P or composition are determined. In order to resemble the standard experimental setup the simulated particle of the porous medium had the shape of a cube with two opposite faces open to the gaseous phase and remaining four faces closed. Boundary conditions of the Dirichlet type were used in the direction of macroscopic transport.

The common approach to solving the system of equations (13) iteratively is a Newton-type method. Since the equations (13) were only mildly non-linear, the Newton method based on line searches converged within a few iterations $(2-5)$. A large sparse system of linear equations arising in each Newton step was solved by a preconditioned biconjugate gradient method (Press et al., 1992).

Diffusion flow in the binary mixture of hydrogen (component A) and nitrogen (component B) was simulated in the three orthogonal directions and for five discrete levels of P in the interval $[100, 500]\,\mathrm{kPa}$. This choice guaranteed that the Knudsen number for hydrogen was less than 0.01 in all chambers and less than 0.09 in the narrowest constriction. The total molar flow rate of hydrogen was related to an area of the cube face. The resulting dependence of the molar flux, N, of hydrogen on P was approximated by a functional relationship, which is commonly used (Scott and Dullien, 1962) for the reduction of experimental data

$$N(P) = \frac{P}{R_g T} \frac{\psi D_{AB}}{\alpha d_p} \ln \frac{1 + \alpha y(0)}{1 + \alpha y(d_p)} \tag{14}$$

where $y(0)$ and $y(d_p)$ are the mole fractions at opposite faces of the cube. The parameter ψ is the ratio of the effective to bulk binary diffusivity. A least-square method (Press et al., 1992) was applied to determine the best estimate of ψ.

4 Comparison with Experiments

Steady-state diffusion experiments were performed in a Wicke-Kallenbach cell operated under the atmospheric pressure. A piece of silicon rubber fastened the cylindrical pellet in a hole drilled in a metallic plate. Each of the open pellet faces were flushed with a different gas stream. The streams of pure gases, involving hydrogen, helium, nitrogen and argon, were fed from pressure cylinders through mass flow controllers. High inlet space velocities were chosen to eliminate the influence of external diffusion resistance. The Wicke-Kallenbach method requires that the total pressures on both sides of the pellet are the same. Otherwise, creeping flow induced by the pressure gradient will affect the diffusion flow. Isobaric conditions were achieved by merging the two outlet gas streams before a vent. Pressure drops in the outlet tubes were adjusted manually in such a way that the pressure difference between the open pellet faces was less than 5 Pa. Downstream from the cell, small amounts of gaseous mixtures were taken away by means of a six-way valve for the analysis of composition.

Equation (14) was also applied to reduce the experimental data. The value of ψ estimated in the least-square sense was found to be 0.123. The random walk-simulator predicted the ratio D_e^m/D^m (10), in which, unlike the experimental quantity, ϕ was not included. Therefore the predicted ratio D_e^m/D^m was multiplied by ϕ resulting in $\psi = 0.102$. The value of 0.129 obtained by modelling diffusion flow in the pore network compares very well with that experimental.

In the case of random-walk simulation the lower value of ψ could stem from a relatively small size of the replica ($256\times256\times256\,\mu\mathrm{m}^3$); therefore, only a few highly penetrable (conductive) pathways connecting the replica faces were likely to exist. On the other hand, the sizes of the pore network and real sample were almost identical so that there could have been approximately the same number of highly penetrable pathways in the pore network like in the real sample. Due to the network connectivity estimated from the stochastic replica the value of $\bar{\omega}$ was likely to be shifted down. However, the lack of highly penetrable pathways could be balanced by enlarging throat sizes during the iterative network construction, which explained the successful prediction of ψ. The correlation of pore space connectivity and the TSD was also observed for a random pore network constituted pores of different geometry (Čapek et al., in press).

For another prediction of ψ, Archie's law can be applied in its simplest form, i.e. $F = \phi^{-2}$ where F is the formation factor. The parameter ψ can be readily determined, because it is inversely proportional to F. This plain calculation gave $\psi = 0.163$, which was less satisfactory than the predictions

obtained by application of the simulators.

5 Conclusions

Stochastic reconstruction of a macroporous $\alpha-$alumina from limited morphological information provided the basis for the construction of a 3D random pore network of irregular topology. Pore network connectivity was characterized by means of the mean coordination number, accessible by the analysis of the reconstructed pore space skeleton. The pore network model and the mercury intrusion simulator enabled the fine adjustment of the throat size distribution according to the experimental mercury intrusion curve. The predictions of effective diffusivities in the stochastic replica and in the random pore network were quite successful: the absolute deviations were less than 18 % of the experimental value. The lower value of the effective diffusivity in the stochastic replica was observed because pore space connectivity was underestimated in the procedure of stochastic reconstruction. The pore network calculation was more successful than the direct calculation of the effective diffusivity because pore network connectivity derived from the stochastic replica could be balanced by enlarging throat sizes. The pore network prediction of the effective diffusivity was also more successful than in our previous paper (Čapek et al., in press) where we employed a pore network of the chamber-and-throat type with throats of constant rectangular cross-section. The convergent-divergent throats, applied here, were more conductive than their counterparts of rectangular cross-section and, therefore, the pore network presented in this study revealed the higher effective diffusivity than the pore network studied in our previous paper (provided that both networks were of the same connectivity). The convergent-divergent throats also more closely resembled the real pore space than those of rectangular cross-section.

Acknowledgments

Financial support from the Grant Agency of the Czech Republic (Research Grant # 203/05/0347) is gratefully appreciated. The authors also thank Prof. Milan Sonka for providing the C code of the thinning algorithm used in this work.

References

Aarts, E., Korst, J., (1989) Simulated Annealing and Boltzmann Machines: A Stochastic Approach to Combinatorial Optimization and Neural Com-

puting. John Wiley & Sons, Chichester.

Baldwin, C. A., Sederman, A. J., Mantle, M. D., Alexander, P., Gladden, L. F., (1996) J. Colloid Interface Sci. 181 (1), 79–92.

Bekri, S., Xu, K., Yousefian, F., Adler, P. M., Thovert, J. F., Muller, J., Iden, K., Psyllos, A., Stubos, A. K., Ioannidis, M. A., (2000) J. Pet. Sci. Eng. 25 (3-4), 107–134.

Bird, R. B., Stewart, W. E., Lightfoot, E. N., (1960) Transport Phenomena. John Wiley & Sons, New York.

Burganos, V. N., (1998) J. Chem. Phys. 109 (16), 6772–6779.

Burganos, V. N., Payatakes, A. C., (1992) Chem. Eng. Sci. 47 (6), 1383–1400.

Čapek, P., Hejtmánek, V., (2004) A relationship between capillary pressure and permeability as revealed by a pore network model. In: 16th International Congress of Chemical and Process Engineering CHISA 2004. Prague, Czech Republic, p. P3.194.

Čapek, P., Hejtmánek, V., Brabec, L., Zikánová, A., Kočiřík, M., (in press) Network modelling of capillary pressure curves, permeability, and diffusivity. Chem. Eng. Sci.

Constantinides, G. N., Payatakes, A. C., (1989) Chem. Engng Commun. 81, 55–81.

Fredrich, J. T., Menendez, B., Wong, T.-F., (1995) Science 268 (5208), 276–279.

Frost, R., Heineman, P., (1997) Simulated annealing: A heuristic for parallel stochastic optimization. In: Arabnia, H. R. (Ed.), PDPTA. CSREA Press, pp. 1595–1604.

Hollewand, M. P., Gladden, L. F., (1992) Chem. Eng. Sci. 47 (7), 1761–1770.

Ioannidis, M. A., Kwiecien, M. J., Chatzis, I., (1997) Transport in Porous Media 29, 61–83.

Johnson, M. F. L., Stewart, W. E., (1965) J. Catal. 4, 248–252.

Kainourgiakis, M. E., Kikkinides, E. S., Galani, A., Charalambopoulou, G. C., Stubos, A. K., (2005) Transport in Porous Media 58, 43–62.

Keil, F. J., (1999) Catal. Today 53, 245–258.

Liang, Z., Ioannidis, M. A., Chatzis, I., (2000a) J. Colloid Interface Sci. 221, 13–24.

Liang, Z., Ioannidis, M. A., Chatzis, I., (2000b) Chem. Eng. Sci. 55 (22), 5247–5262.

Manwart, C., Hilfer, R., (1999) Phys. Rev. E 59 (5), 5596–5599.

Mason, E. A., Evans III, R. B., (1969) J. Chem. Educ 46 (6), 358–364.

Mason, E. A., Malinauskas, A. P., Evans III, R. B., (1967) J. Chem. Phys. 46 (8), 3199–3216.

Mason, E. A., Marrero, T. R., (1972) J. Phys. Chem. Ref. Data 1 (1), 1–118.

Min Ma, C., Sonka, M., (1996) Computer Vision and Image Understanding 64 (3), 420–433.

Press, W. H., Teukolsky, S. A., Vetterling, W. T., Flannery, B. P., (1992) Numerical Recipes in C: The Art of Scientific Computing, 2nd Edition. Cambridge University Press, Cambridge.

Sahimi, M., (1995) Flow and Transport in Porous Media and Fractured Rock: From Classical Methods to Modern Approaches. VCH, Weinheim, Germany.

Sahimi, M., Gavalas, G. R., Tsotsis, T. T., (1990) Chem. Eng. Sci. 45 (6), 1443–1502.

Sahimi, M., Stauffer, D., (1991) Chem. Eng. Sci. 46 (9), 2225–2233.

Scott, D. S., Dullien, F. A. L., (1962) A.I.Ch.E. J. 8 (1), 113–117.

Spanne, P., Thovert, J. F., Jacquin, C. J., Lindquist, W. B., Jones, K. W., Adler, P. M., (1994) Phys. Rev. Lett. 73 (14), 2001–2004.

Talukdar, M. S., Torsaeter, O., Ioannidis, M. A., Howard, J. J., (2002) J. Pet. Sci. Eng. 35 (1-2), 1–21.

Thovert, J. F., Salles, J., Adler, P. M., (1993) J. Microsc. 170, 65–79.

Torquato, S., (2002) Random Heterogeneous Materials: Microstructure and Macroscopic Properties. Springer-Verlag, New York.

Tsakiroglou, C. D., Payatakes, A. C., (1990) J. Colloid Interface Sci. 137 (2), 315–339.

Tsakiroglou, C. D., Payatakes, A. C., (1991) J. Colloid Interface Sci. 146 (2), 479–494.

Tsakiroglou, C. D., Payatakes, A. C., (1993) J. Colloid Interface Sci. 159 (2), 287–301.

Tsakiroglou, C. D., Payatakes, A. C., (2000) Adv. Water Resour. 23, 773–789.

Yeong, C. L. Y., Torquato, S., (1998a) Phys. Rev. E 58 (1), 495–506.

Yeong, C. L. Y., Torquato, S., (1998b) Phys. Rev. E 58 (1), 224–233.